

Searching for Saddle Points by Using the Nudged Elastic Band Method: An Implementation for Gas-Phase Systems

Núria González-García,^{†,‡} Jingzhi Pu,[†] Àngels González-Lafont,[‡] José M. Lluch,[‡] and Donald G. Truhlar^{*,†}

Departament de Química, Universitat Autònoma de Barcelona, 08193 Bellaterra, Barcelona, Spain, and Department of Chemistry and Supercomputing Institute, University of Minnesota, 207 Pleasant Street Southeast, Minneapolis, Minnesota 55455-0431

Received January 27, 2006

Abstract: A new implementation of the Nudged Elastic Band (NEB) optimization method is presented. This approach uses a global procedure that yields the whole reaction path, and thus it provides an alternative to the sequential optimization of the transition state and consequent calculation of the minimum energy path. Furthermore the algorithm is very useful when one is not sure if a saddle point exists, because it can be used to eliminate the possibility of a saddle point when one does not exist. Three different versions of the NEB algorithm have been implemented. The influences of various parameters and methodological choices on the performance of the method have been studied, and the quality of the results is assessed by comparison with the saddle point and minimum energy path calculations sequential method. Recommendations are made for algorithmic choices and default parameters.

1. Introduction

Characterization of the potential energy surface (PES) is a key step in the study of any reaction. In most cases, all detailed information about the PES is obtained from electronic structure calculations.^{1,2} The steps that are usually followed to characterize a PES are, first, locating the minima and saddle points on the PES and, second, calculating the reaction paths connecting those stationary points.^{3–6} Finding the saddle points (SPs) can be especially difficult for large systems, even in the gas phase. In many cases the decisive factor in this search is to start with a good guess, which can be obtained by many different procedures such as by analogy to previously studied systems, by finding the maximum-energy structure along an approximate reaction coordinate, by performing partial optimizations, or by carrying out a full optimization at a lower level of theory where one can afford to calculate multiple Hessians to guide the search. But even

using multiple Hessians or a good guess, this search can fail. Once the SP is optimized and characterized, the minimum energy path (MEP) can be calculated.

Many different methods have been presented for finding saddle points and reaction paths.^{3–24} Some reaction paths just provide a good guess to start a search for the saddle point. One of these methods is the distinguished reaction coordinate method,⁹ where one degree of freedom, called the distinguished coordinate, is chosen and kept fixed at a sequence of values, while all the other coordinates are relaxed for each of these values. The value of the distinguished coordinate is incremented in a stepwise fashion, and the system is dragged from reactants to products. The maximum-energy geometry along the path is taken as the initial guess for the saddle-point search. The intuitively assumed reaction coordinate can turn out to be a bad one, although some authors have developed methods that overcome some of the disadvantages of the distinguished reaction coordinate method.^{25,26} Another useful algorithm for finding saddle points is the eigenvector following (EF) method.^{10–14} This algorithm starts from a local minimum and follows the most

* Corresponding author e-mail: truhlar@umn.edu.

[†] University of Minnesota.

[‡] Universitat Autònoma de Barcelona.

gradually ascending generalized-normal-mode eigenvector, step by step, until reaching the saddle point. Once the saddle point is characterized, the EF algorithm can be used to trace the MEP from the saddle point to the minima it connects; the first step in such a process is to follow the unique descending eigenvector at the saddle point. Unfortunately, obtaining the generalized-normal-mode eigenvectors by diagonalizing the Hessian matrix requires expensive computations so that this method is only viable for small systems or low levels of electronic structure theory.

A promising alternative to these traditional methods is provided by a group of methods that may be classified as chain-of-states methods. In these methods, a path is represented by a set of discrete structures forming a chain of replicas of the system. The structures, called images, are then optimized to try to make the entire chain lie on the MEP. Since the MEP passes through the saddle point, these methods simultaneously locate the SP and the MEP. The Nudged Elastic Band (NEB) method^{15–24} is an example of this chain-of-states approach. The NEB method can be used either as an alternative to traditional methods when they fail or as an inexpensive way to characterize the PES. A key advantage of the NEB is that it provides a global search, whereas many traditional methods only converge in the vicinity of a good initial guess.

The present article presents some illustrations of the NEB method based on a new implementation in an electronic structure code, namely MULTILEVEL.²⁷ The implementation requires only two or three initial geometries, which are provided by the user, and after generating an initial path, the program will optimize it to the MEP. Alternatively the initial steps of the NEB minimization can be used to provide a good initial guess for a more traditional TS search.

Section 2 describes the NEB method and reviews some of the previous implementations. Section 3 tests the new implementation for several reactions and recommends a version that performs quite well along with a set of default values for several of the parameters of the method. The systems used are all related to dimethyl sulfide (DMS) degradation in the atmosphere. DMS is thought to be the major biogenic component of the global atmospheric budget. The potential role of DMS in global climate change has been a subject of considerable controversy; it has been suggested that a biological/chemical cycle based on DMS could form the basis of an efficient method of climate regulation.²⁸ Previous work on DMS and the hydroxyl radical has been published,^{29,30} and here we apply the NEB technique to some unsolved questions on reactions in that degradation scheme that had not been studied yet.

2. The Nudged Elastic Band Method

2.1. Theory. In the Nudged Elastic Band (NEB) method,^{15,16,19} the reaction path is described by a discrete sequence of images consisting of two fixed end points (\vec{R}_0 and \vec{R}_{n+1}) and n intermediate movable images ($\vec{R}_1, \vec{R}_2, \dots, \vec{R}_n$). This sequence is called the chain or the elastic band. Spring interactions are added between adjacent images. The total force (also called the adjusted force) acting on each image is the sum

of the spring force \vec{F}_i^s and the force \vec{F}_i^t from the potential energy surface (which will be called the true force). The band is optimized, minimizing the total force acting on each image. During this process, the true force tends to pull the images toward the end points, giving the lowest resolution in the region nearest to the saddle point. This behavior is known as the sliding-down phenomenon. On the other hand, corner cutting is induced by the spring force pulling the sequence of images to the concave side of the MEP in the regions where it is curved. These two problems are solved by projecting out the component of the true force parallel to the chain of images and the component of the spring force perpendicular to the chain.

Then the adjusted force acting on an image, i , is given by

$$\vec{F}_i = \vec{F}_{i\parallel}^s + \vec{F}_{i\perp}^t \quad (1)$$

which is the sum of the spring force along the tangent to the chain and the true force perpendicular to the chain. The parallel component of the spring force, in the first version of the method,^{15,16,19} is calculated as

$$\vec{F}_{i\parallel}^s = \{k[(\vec{R}_{i+1} - \vec{R}_i) - (\vec{R}_i - \vec{R}_{i-1})] \cdot \hat{\tau}_i\} \hat{\tau}_i \quad (2)$$

where k is the spring constant and $\hat{\tau}_i$ is the unit tangent vector at an image i . Furthermore, in the original version, the tangent is estimated by using the normalized line segment between two nonadjacent images along the path, \vec{R}_{i+1} and \vec{R}_{i-1}

$$\hat{\tau}_i = \frac{\vec{R}_{i+1} - \vec{R}_{i-1}}{|\vec{R}_{i+1} - \vec{R}_{i-1}|} \quad (3)$$

but a slightly better way^{15,19,20} is to bisect the two unit vectors

$$\tau_i^{(0)} = \frac{\vec{R}_i - \vec{R}_{i-1}}{|\vec{R}_i - \vec{R}_{i-1}|} + \frac{\vec{R}_{i+1} - \vec{R}_i}{|\vec{R}_{i+1} - \vec{R}_i|} \quad (4a)$$

and then normalize so that

$$\hat{\tau}_i = \tau_i^{(0)} / |\tau_i^{(0)}| \quad (4b)$$

Using eqs 4a and 4b to define the tangent ensures that the images are equally spaced (when the spring constant k is the same for each adjacent pair) even in regions of large curvature of the path. This last way of estimating the tangent will be called the bisection NEB or B-NEB version of the NEB algorithm in this work. The tangent vector is also used to obtain the perpendicular component of the true force

$$\vec{F}_{i\perp}^t = \vec{F}_i^t - (\vec{F}_i^t \cdot \hat{\tau}_i) \hat{\tau}_i \quad (5)$$

In systems where the force along the minimum energy path is large compared to the restoring force perpendicular to the path, the system can develop kinks, preventing the band from converging to the MEP. At kinks the angle between the vectors $\vec{R}_i - \vec{R}_{i-1}$ and $\vec{R}_{i+1} - \vec{R}_i$ is large, so that including some fraction of the perpendicular component of the spring force may tend to straighten the elastic band.¹⁹

An improved estimation of the tangent was proposed²⁰ to eliminate kinks. Instead of using both adjacent images, $i + 1$ and $i - 1$, just the image with the highest energy is used for the estimation of the tangent at image i . The new tangent,

which replaces eq 4a, is

$$\tau_i^{(0)} = \begin{cases} \tau_i^+ & \text{if } V_{i+1} > V_i > V_{i-1} \\ \tau_i^- & \text{if } V_{i+1} < V_i < V_{i-1} \end{cases} \quad (6a)$$

where

$$\tau_i^+ = \vec{R}_{i+1} - \vec{R}_i \text{ and } \tau_i^- = \vec{R}_i - \vec{R}_{i-1} \quad (6b)$$

and V_i is the potential energy, $V(\vec{R}_i)$, of image i . If both adjacent images are either lower or higher in energy than image i , then the tangent is taken to be a weighted average of the vectors to the two neighboring images. This weight is determined from the energy. The weighted average only plays a role at extrema along the MEP, and it serves to smoothly switch between the two possible tangents $\hat{\tau}_i^+$ and $\hat{\tau}_i^-$; otherwise, there is an abrupt change in the tangent as one image becomes higher in energy than another, and this can lead to convergence problems. If image i is at a minimum ($V_{i+1} > V_i < V_{i-1}$) or at a maximum ($V_{i+1} < V_i > V_{i-1}$), then the tangent estimate becomes

$$\tau_i^{(0)} = \begin{cases} \tau_i^+ \Delta V_i^{\max} + \tau_i^- \Delta V_i^{\min} & \text{if } V_{i+1} > V_{i-1} \\ \tau_i^+ \Delta V_i^{\min} + \tau_i^- \Delta V_i^{\max} & \text{if } V_{i+1} < V_{i-1} \end{cases} \quad (7a)$$

where

$$\Delta V_i^{\max} = \max(|V_{i+1} - V_i|, |V_{i-1} - V_i|) \quad (7b)$$

and

$$\Delta V_i^{\min} = \min(|V_{i+1} - V_i|, |V_{i-1} - V_i|) \quad (7c)$$

Finally, the tangent vector needs to be normalized, using eq 4b. With this modified tangent, the elastic band is well behaved and should converge rigorously to the MEP if a sufficient number of images are included in the band. Another modification included in the same version^{20,18} of the NEB method that introduced eqs 6 and 7 is the evaluation of an improved spring force:

$$\vec{F}_{\text{all}}^s = k(|\vec{R}_{i+1} - \vec{R}_i| - |\vec{R}_i - \vec{R}_{i-1}|)\hat{\tau}_i \quad (8)$$

This new definition of the spring force, when used instead of eq 2, ensures equal spacing of the images when the same spring constant, k , is used for the springs even in regions of high curvature where the angle between $\vec{R}_i - \vec{R}_{i-1}$ and $\vec{R}_{i+1} - \vec{R}_i$ is large. This version of the NEB defined by eqs 6–8 is called improved tangent NEB or IT-NEB.

Another modification of the NEB, called Climbing Image NEB: CI-NEB,¹⁸ has been introduced for the purpose of using an NEB calculation to converge a saddle point. This new method modifies the definition of the total force on the highest-energy image after a few iterations. After identifying this image as point i_{\max} , the force on i_{\max} is given not by eq 1, but rather by

$$\vec{F}_{i_{\max}} = -\nabla V(\vec{R}_i) + 2\nabla V(\vec{R}_i)|_{\parallel} = -\nabla V(\vec{R}_i) + 2(\nabla V(\vec{R}_i) \cdot \hat{\tau}_i)\hat{\tau}_i \quad (9)$$

The highest energy image, i_{\max} , is not affected by the spring forces at all. The total force acting on all the other images

is still defined by eq 1 (as in B-NEB and IT-NEB), and the definition of the tangent and the spring force are still given by eqs 6–8 (as in IT-NEB). The CI-NEB algorithm should converge to the saddle point more efficiently than either B-NEB or IT-NEB.

2.2. Implementations. 2.2.1. G98+NEB. As far as we know, the only NEB implementation that has been made available in a distributed computer program for gas-phase systems is the one implemented by Alfonso and Jordan.²² The driver is called *G98+NEB*, and it performs NEB calculations using energies and forces obtained from the *Gaussian98* package.³¹ The driver consists of the NEB code and several script files that mediate the information flow between the NEB code and the *Gaussian98* program. In addition, it includes utility codes to generate the initial points via linear interpolation. The basic *G98+NEB* procedure can be summarized as follows:

(i) By using a utility code, an N -point approximation of the path is generated using linear interpolation in Cartesian coordinates between the two end points.

(ii) The energy and force for each movable image as well as at the end points are computed by calling *Gaussian98*.

(iii) Spring interactions with spring constant k between adjacent images are added, and the tangent is computed by the IT-NEB algorithm.

(iv) The corresponding projections of the true and parallel forces are computed by using the previously calculated tangent vectors, using eq 8.

(v) The points in the elastic band are brought to the nearest MEP via minimization of the adjusted NEB forces. This can be done using conventional minimization techniques such as the steepest descent or modified Broyden³² method or by using damped dynamics procedures.

2.2.2. MULTILEVEL4.1. Our implementation of the NEB method has been incorporated in the MULTILEVEL program.²⁷ This implementation follows the global scheme depicted in Figure 1. This diagram can be compared with the one used in the *G98+NEB* program depicted in ref 22. The first important difference between our implementation and the one previously described is the way in which the initial set of images is generated. The *Interpolation* utility in the *G98+NEB* package can lead to an unphysical chain if the user does not start with physically consistent orientations for the two end points. In MULTILEVEL4.1 an initial reorientation of the two end points is performed by Chen's algorithm,³³ adopting the implementation from the *PolyRate* package.³⁴ After this reorientation, the initial set of images is generated by linear interpolation in Cartesian coordinates. However, the user can supply an external file containing all n movable images plus the two end points, and the program will read it and avoid the two previous steps.

Once the initial set of images is generated, the program enters subroutine NEBGHK. First, the potential energies V_i are calculated for all images, and the corresponding gradients are calculated for all images except the two end points. After this, the local tangent is evaluated, and the projections of the true and spring forces are carried out. Both the B-NEB¹⁵ and the newer²⁰ (IT-NEB) definitions for these two variables (the tangent and the spring force) have been implemented.

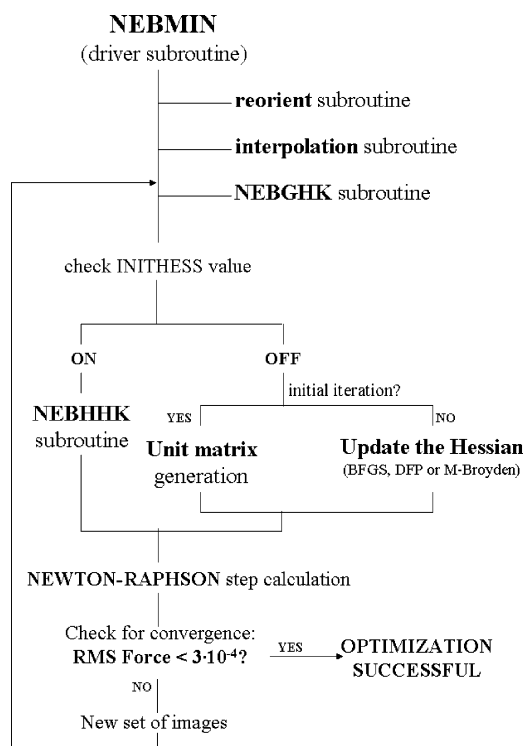


Figure 1. Flow diagram of the implementation of the NEB in the MULTILEVEL package. Note that INITHESS can be switched on or off depending on the way that the initial Hessian is obtained. If it is on, the initial Hessian will be calculated, while if is off, the initial Hessian will be approximated by a scaled unit matrix.

However, the default options correspond to eqs 6–8 (IT version) because it was demonstrated by Jónsson and co-workers²⁰ that the previous ones can promote the formation of kinks along the band. The CI algorithm is also implemented, and it uses the same formulation for these variables (tangent and spring forces) as the IT option. It just modifies the total force acting on the highest energy image after a few iterations, which is taken as five iterations in our implementation. This number was chosen after verifying that the highest energy image at this iteration remains the same along all the following minimization cycles in the tests we have made.

Finally subroutine NEBGHK calculates the adjusted force vector \vec{F} (see eq 1) which collects the $M \vec{F}_i$, where M is the number of images. The components of the resulting vector \vec{F} , of order $M \times 3N$ (where N is the number of atoms of the system), will be minimized using one of the available quasi-Newton methods.

The quasi-Newton optimization methods available in MULTILEVEL-v4.1 are variations of the Newton–Raphson method where an approximate Hessian matrix (or its inverse) is gradually updated using the gradient and displacement vectors of the previous steps.^{35–42} The displacement that is performed to move toward a stationary point is given by

$$\Delta \vec{q}_k = -H_k^{-1} \vec{g}_k \quad (10)$$

where \vec{g}_k is minus the adjusted force vector corresponding to iteration k , and the elements in H_k^{-1} should be obtained

from the derivatives of the gradient components. The possibility of obtaining the exact inverse Hessian H_k^{-1} corresponding to the adjusted force vector is implemented in our program only for the B version of the NEB algorithm. However, this process is computationally very expensive, and to avoid it another strategy will be followed.

The first option that must be set by the user is the choice of methods for calculating the initial Hessian. The user can choose between three different possibilities: using a scaled unit matrix, a low-level initial Hessian, or a high-level initial Hessian. A low-level Hessian means that the force constant matrix is evaluated at a lower electronic level than the gradients derived from the potential energy V_i . A high-level Hessian implies that the Hessian would be calculated at the same electronic level as the energies and gradients previously obtained.

During the minimization cycles, the Hessian can be recalculated or updated. Furthermore, the number of cycles after which the Hessian is to be recalculated must be defined by the user. Between two recalculations, the Hessian H_k is kept frozen. There are various possibilities for updating the Hessian H_k during the minimization cycles: the BFGS algorithm,^{36–39} the Davidson–Fletcher–Powell (DFP) algorithm,⁴³ or the Modified Broyden method,³² as described by Alfonso and Jordan.²² The quasi-Newton methods generate new geometries (by eq 10) that form the initial chain to start another minimization cycle. This process is repeated until the convergence criterion is satisfied.

These procedures are the same for the CI-NEB¹⁸ option except that the definition of the total force acting on the highest energy image which will be given by eq 9 after five iterations.

The default convergence criterion is based on the root-mean-square of the components of the true force acting on the whole band. This value is required to be smaller than or equal to $3 \cdot 10^{-4}$ hartrees per bohr ($E_h a_0^{-1}$), which is the same default convergence criterion used by *Gaussian03*⁴⁴ in optimizations.

Another key parameter which may be monitored along the optimization is the maximum component of the adjusted force at the highest energy image. As this image is supposed to converge to the saddle point, the true force should approach zero. This feature will be used as the criterion to determine the “best” parameters for each option that can be controlled by the user.

3. Calculations, Results, and Discussion

3.1. Testing Various Options. With the aim of determining good default values for the various options of the program, we tested them for the H-abstraction from CH_4 by the hydroxyl radical. To build the initial sequence of images, we used three structures: the ones corresponding to the van der Waals complexes in the entrance and exit channels (named *wellR* and *wellP*, respectively) and an intermediate structure, where the distance between the oxygen in the OH and one of the hydrogens in the methane is 1.2 Å. This distance would be a reasonable starting value for saddle points where an OH is abstracting a hydrogen. An initial

reorientation of the three structures (*wellR*, intermediate structure, and *wellP*) is carried out followed by two linear interpolations: from *wellR* to the intermediate point and from the intermediate point to *wellP*. The new structures obtained from each interpolation plus the intermediate structure, included as another movable image, formed the initial guess of movable images.

The program does not automatically carry out the interpolations mentioned in the previous paragraph; they must be done manually, and the initial set of movable images is then supplied by the user in an external file.

The electronic-structure level chosen for these tests was density functional theory with the modified Perdew-Wang 1-parameter functional for kinetics: MPW1K.⁴⁵ (This functional was optimized⁴⁵ to a database of barrier heights and reaction energies. Several studies have demonstrated that the MPW1K functional gives good performance for kinetics.^{46–50} However, the increased percentage of Hartree–Fock exchange in MPW1K deteriorates the atomization energy calculation.⁴⁵) The 6-31+G(d,p) basis set^{51,52} was chosen as a good compromise between cost and efficiency for the system studied. To compare the performance of the various options, we always performed 40 iterations, and then the maximum component of adjusted force at the highest energy image was checked. As the NEB algorithm should converge to the SP, the forces at the highest energy image should go to zero.

The parameters we will test here are: the number of images, the choice of B, IT, or CI for the NEB algorithm, the way of generating the initial Hessian to obtain the displacement during the quasi-Newton minimization, how to update this Hessian as the optimization proceeds, and the spring constant. Other parameters that can be controlled by the user are not tested here. Examples would be inclusion of some intermediate points (apart from the two fixed end points) in order to generate the initial chain, calculation of a new full Hessian along the minimization, etc.

We started our study using some reference values of the parameters taken from previous work. For example, we used a value for $k_{\text{spring}} = 0.02 \text{ E}_h\text{a}_0^{-2}$ as recommended by Alfonso and Jordan,²² and we used a scaled unit matrix as initial Hessian with $\text{HSCALE} = 100 \text{ E}_h\text{a}_0^{-2}$ (see below for the definition of HSCALE). Due to the arbitrariness of these parameters, we performed an iterative determination of the optimum parameters; that is, once we obtained the best value for one parameter, we reoptimized all the others. In this way, we could obtain best parameters even if their optimum values are coupled. The intermediate results of this iterative optimization are not discussed, and we will just discuss the final results. Figures 2–5 show the results after 40 steps of path minimization for various values of each parameter, and Table 1 gives the corresponding values for the maximum component of the adjusted force at the highest energy image (the criterion followed to decide the best parameters).

3.1.3. Number of Images. The number of images to be used in carrying out the NEB minimization should depend on the objectives of the user. For example, if one is using the NEB method just to obtain the qualitative nature of the path from reactants to products and to check if there is an energy maximum along this path, a small number of images

Table 1: Influence of the Various Parameters on the NEB Minimization^a

variable	variable value	maximum component ($\text{E}_h\text{a}_0^{-1}$)	
		iteration 20	iteration 40
n^b	11	0.0280	0.0219
	21	0.0282	0.0229
	41	0.0277	0.0228
HSCALE ($\text{E}_h\text{a}_0^{-2}$)	1	0.0048	0.0048
	10	0.0229	0.0056
	10 ²	0.0283	0.0222
	10 ³	0.0302	0.0258
NEB algorithm	B-NEB	0.0373	0.0341
	IT-NEB	0.0255	0.0202
	CI-NEB	0.0229	0.0056
update scheme	BFGS	0.0229	0.0056
	DFP	0.0297	0.0288
	mBroyden	0.0301	0.0271
k_{spring} ($\text{E}_h\text{a}_0^{-2}$)	1	0.0305	0.0162
	10 ⁻¹	0.0195	0.0142
	10 ⁻²	0.0229	0.0056
	10 ⁻³	0.0234	0.0059
	10 ⁻⁴	0.0234	0.0059

^a The absolute value of the maximum component of the adjusted force at the highest energy image (in atomic units: $\text{E}_h\text{a}_0^{-1}$) at iterations 20 and 40, respectively, is used as a test for the convergence of the method. The rows corresponding to recommended values are in bold. In each case, when one parameter or choice is varied, the other four are fixed at their recommended value, except for the first 3 rows in the table. That row has $n = 11$, HSCALE = 100 $\text{E}_h\text{a}_0^{-2}$, NEB choice = CI-NEB, update scheme = BFGS, and $k_{\text{spring}} = 0.02 \text{ E}_h\text{a}_0^{-2}$. ^b n is the number of movable images.

can be used. However, if the user wants to tightly optimize the saddle point, more images should be included. However, the most efficient way to get an accurate saddle point would be to carry out the NEB minimization in more than one cycle: one could start using a few images just to locate the maximum energy region. Then, with that region defined, we would run a second NEB minimization concentrating all the images in the area surrounding the saddle point. In this way, the highest-energy image can be made to approach closer and closer to the saddle point. Various kinds of interpolation could be done between the three highest-energy images in order to obtain a better geometry for the saddle point; for example, the user can apply a quadratic interpolation.

We tested the performance for $n = 11$, 21, and 41 movable images. These numbers include 5, 10, or 20 interpolated images plus the intermediate image that is included. All of the images were obtained by using the same initial points, as explained above; we just increased the number of points generated between them. In Table 1 the maximum component of the adjusted force at the highest energy image are shown. As can be seen, the results do not depend strongly on the number of images used. Therefore, for the H-abstraction in the $\text{CH}_4 + \text{OH}$ system, 11 movable images provide a good compromise between cost and accuracy. This option was not reoptimized with the best values for the other parameters, and in Table 1 the results shown correspond to those obtained with the values recommended by Alfonso and Jordan.²²

For all the tests presented in the rest of section 3.1, we set $n = 11$ except in Table 1, which also shows results for $n = 21$ and 41.

3.1.2. Scaled Unit Matrix. Using a unit matrix as an approximate initial Hessian is well-known to be an efficient

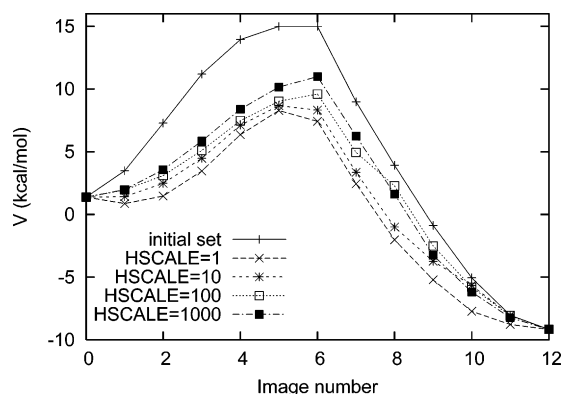


Figure 2. Influence of the HSCALE ($E_h a_0^{-2}$) value used in the minimization for $\text{CH}_4 + \text{OH}$ system. All other variables were kept unchanged: CI-NEB algorithm, $k_{\text{spring}} = 0.01 E_h a_0^{-2}$, and BFGS update scheme. The relative potential energy (vs reactants) is depicted vs the image number at iteration 40. The “initial set” stands for the energy at the initial chain of images.

way to obtain the displacement in quasi-Newton minimizations. This unit matrix can be scaled in order to obtain a matrix closer to the real Hessian. The value used will be named HSCALE (as the unit matrix has no units, the HSCALE gives dimension to that matrix in order to adjust it to approximate a Hessian). We tested several values for this variable, and the results are shown in Figure 2. The values for the maximum component of the adjusted force at the highest energy image can be seen in Table 1. In all the cases, the other three parameters were kept fixed at the values: CI-NEB algorithm, BFGS update scheme, and $k_{\text{spring}} = 0.01 E_h a_0^{-2}$. Although the options $\text{HSCALE} = 10^{-2} E_h a_0^{-2}$ and $\text{HSCALE} = 10^4 E_h a_0^{-2}$ were also tested, we do not show the results; both values yield a band that does not minimize correctly. The smallest value ($\text{HSCALE} = 10^{-2} E_h a_0^{-2}$) gave an initial quasi-Newton step (see eq 10) so large that the displacement moved the new set of images very far away from the initial one, and the energies did not minimize. On the other hand, the largest value ($\text{HSCALE} = 10^4 E_h a_0^{-2}$) gave a very small initial quasi-Newton step so that the next set of images was almost equal to the initial one. The intermediate values for HSCALE perform quite well, but the best option is HSCALE equal to $1 E_h a_0^{-2}$.

One could choose other options for the initial Hessian. For example, the program could compute the “true” force constant matrix (at the actual electronic level or lower) for each image in the set of images. The calculated Hessian corresponds to the “true” Hessian of the system without spring forces; i.e., without the terms representing the interactions between images; recall that the gradient in eq 10 is the “total” gradient (also called “adjusted” gradient), not the “true” gradient. In fact, and probably for this reason, this option did not work better than the scaled unit matrix.

The third option, the use of exact Hessians (as defined in eq 10), cannot be recommended either; especially when one takes into account the computational cost to compute the Hessian, which is $(M \times 3N) \times (M \times 3N)$, where N is the number of atoms of the system and M is the number of

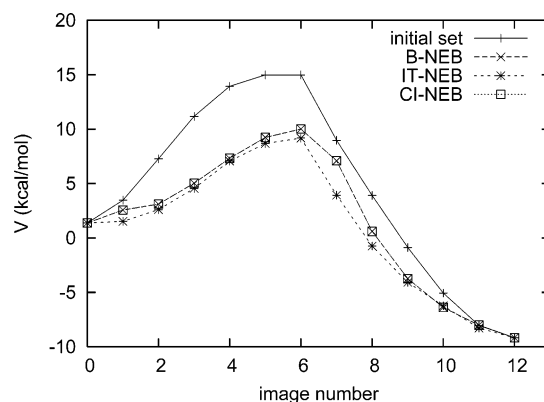


Figure 3. Influence of the iterative process chosen in the minimization for $\text{CH}_4 + \text{OH}$ system. All other variables were kept unchanged: BFGS update scheme, $k_{\text{spring}} = 0.01 E_h a_0^{-2}$, and $\text{HSCALE} = 10 E_h a_0^{-2}$. The relative potential energy (vs reactants) is depicted vs the image number at iteration 40. The “initial set” stands for the energy at the initial chain of images.

images. Nevertheless, MULTILEVEL4.1 does have an option to use the exact Hessian if the user chooses the B-NEB algorithm. In this case, the Hessian also contains the off-diagonal terms corresponding to the spring forces. These terms involve the tangent vector, and they are easier to derive for B-NEB than for IT-NEB or CI-NEB. This option, however, is computationally more expensive than the scaled unit matrix and hence is not recommended either.

To summarize, we recommend using a scaled unit matrix with $\text{HSCALE} = 1\text{--}10 E_h a_0^{-2}$ in order to start the NEB minimization.

3.1.3. Iterative Process. Three different versions of the iterative scheme in the NEB algorithm were implemented: B-NEB,¹⁵ IT-NEB,²⁰ and the CI-NEB.¹⁸ All the other options were fixed for the three tests by employing k_{spring} equal to $0.01 E_h a_0^{-2}$ and a scaled unit matrix as a initial Hessian, with $\text{HSCALE} = 10 E_h a_0^{-2}$. The results are depicted in Figure 3. The values of the maximum component of the adjusted force at the highest energy image listed in Table 1 show small differences between the three options. Although these differences are small, the CI-NEB performed better than the other ones, as was expected due to its special design for SP optimizations.

3.1.4. Update Scheme. The initial Hessian matrix was approximated by a scaled unit matrix. However, during the optimization of the path, this matrix can be and is updated by using one of the three possible schemes: BFGS,^{36–39} DFP,⁴³ or modified Broyden.³² We compared the performance of these three algorithms; in all cases we used a scaled unit matrix as an initial Hessian with $\text{HSCALE} = 10 E_h a_0^{-2}$, the CI-NEB algorithm was used, and k_{spring} was set equal to $0.01 E_h a_0^{-2}$. The results obtained are depicted in Figure 4. As can be seen, after 40 iterations, the BFGS algorithm gives the best converged path, followed by the modified Broyden algorithm. Since the computational costs for these three schemes are very similar, we recommend using BFGS. Table 1 shows that the maximum components of the adjusted force at the highest energy image confirm the better performance of the BFGS update scheme.

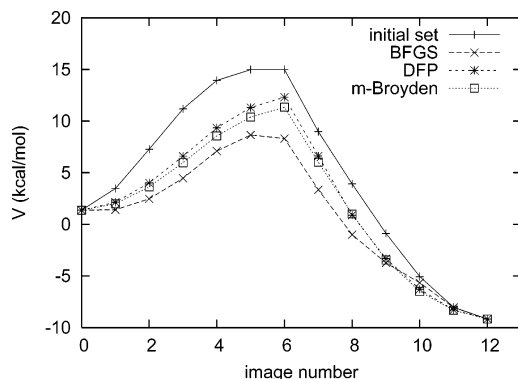


Figure 4. Influence of the update scheme used in the minimization for $\text{CH}_4 + \text{OH}$ system. All other variables were kept unchanged: CI-NEB algorithm, $k_{\text{spring}} = 0.01 \text{ E}_{\text{h}}\text{a}_0^{-2}$, and $\text{HSCALE} = 10 \text{ E}_{\text{h}}\text{a}_0^{-2}$. The relative potential energy (vs reactants) is depicted vs the image number at iteration 40. The “initial set” stands for the energy at the initial chain of images.

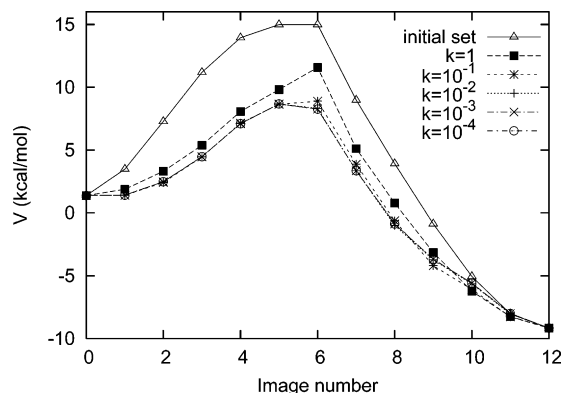


Figure 5. Influence of the $k_{\text{spring}} (\text{E}_{\text{h}}\text{a}_0^{-2})$ value used in the minimization for $\text{CH}_4 + \text{OH}$ system. All other variables were kept unchanged: CI-NEB algorithm, $\text{HSCALE} = 10 \text{ E}_{\text{h}}\text{a}_0^{-2}$, and BFGS update scheme. The relative potential energy (vs reactants) is depicted vs the image number at iteration 40. The “initial set” stands for the energy at the initial chain of images.

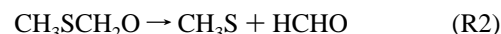
Note that the update scheme needed in the NEB is qualitatively different from the update schemes needed in searching for saddle points in a quasi-Newton procedure. In a quasi-Newton procedure, one can use special update schemes for Hessians that contain a negative eigenvalue.⁴¹ However, for the NEB calculation, we are minimizing all the components of the total force, and the Hessian should not contain any negative eigenvalue.

3.1.5. Spring Constant. To test the influence of the value of the spring constant on the performance of the NEB minimization, we used many different values. For these tests, the CI-NEB and the BFGS choices were used as the iterative process and update scheme, respectively, and a scaled unit matrix with $\text{HSCALE} = 10 \text{ E}_{\text{h}}\text{a}_0^{-2}$ was used as initial Hessian. The results obtained for NEB minimization after 40 iterations are depicted in Figure 5, and the maximum components of the adjusted force at the highest energy image are shown in Table 1. As can be seen, using a large value for the k_{spring} results in very poor performance of the

algorithm. This occurs because the global force on each image is almost totally due to the spring force. The best value for k_{spring} is $0.01 \text{ E}_{\text{h}}\text{a}_0^{-2}$.

3.2. Tests. In this section, we will present some tests of the method on various systems. Based on the studies presented in section 3.1, we used the following options to characterize the paths in these test applications: (i) spring constant: $0.01\text{--}0.001 \text{ E}_{\text{h}}\text{a}_0^{-2}$; (ii) scaled unit matrix as initial Hessian ($\text{HSCALE} = 1\text{--}10 \text{ E}_{\text{h}}\text{a}_0^{-2}$); (iii) update scheme: BFGS; (iv) NEB algorithm: CI-NEB; and (v) n (number of movable images): depending on the purpose of the user ($10\text{--}15$ in order to obtain a good initial guess). When the points in the NEB profile are closer, the reaction path is smoother.

The radicals CH_3SO_2 and $\text{CH}_3\text{SCH}_2\text{O}$ are key species formed in the addition and abstraction mechanisms, respectively, of the $\text{DMS} + \text{OH}$ reaction.⁵³ There are no theoretical studies of the pathways of their dissociations. However, these dissociations are potentially important because the final products are directly linked to SO_4^{2-} formation⁵³



The other reaction chosen is also part of the abstraction mechanism, and it involves a heavy-atom transfer:



It has been proposed that this reaction takes place via an intermediate:⁵⁴



The main aim in studying these reactions was to obtain a global knowledge of the path: does the reaction take place via a saddle point or does the energy along the MEP change monotonically. One possibility to answer those questions would be to perform an NEB minimization. Furthermore, if a maximum along the NEB profile appeared, we could then refine that NEB minimization in order to get closer to the saddle point. The electronic-structure level chosen was again the MPW1K density functional method⁴⁵ for the reasons explained above. Moreover, it has been shown that this functional works well for these kind of reactions.²⁹

3.2.1. CH_3SO_2 and $\text{CH}_3\text{SCH}_2\text{O}$ Dissociations. The initial guess of images for both reactions R1 and R2 was built by direct interpolation from the minima (CH_3SO_2 and $\text{CH}_3\text{SCH}_2\text{O}$, respectively) to a “product-like” structure. For reaction R1, we used an end point where the C–S distance was 3 \AA , while for reaction R2, that distance was 4.5 \AA . The end points with stretched bonds were not optimized. The results for both reactions are depicted in Figure 6.

The top half of Figure 6 shows that the CH_3SO_2 dissociation does not present any maximum of energy along the NEB. It is reasonable to conclude that this dissociation takes place by a monotonic increase in the energy, so searching for a saddle point would be fruitless. The same conclusion could be reached by computing a distinguished reaction-

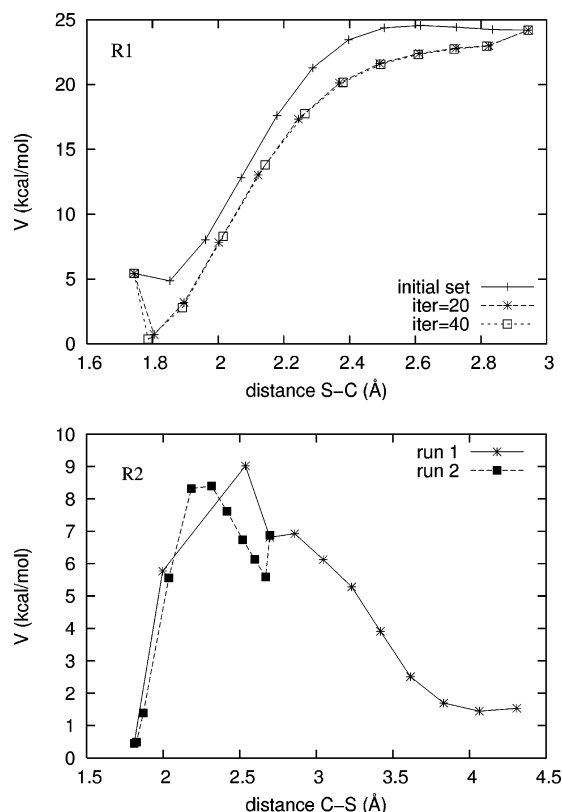


Figure 6. NEB minimization for CH_3SO_2 (top) and CH_3SCH_2O (bottom) systems. Top: Relative potential energy (vs reactant, CH_3SO_2) vs breaking bond distance (d_{S-C}) after 20 and 40 iterations (just one run was performed). Bottom: Relative potential energy (vs reactant, CH_3SCH_2O) vs breaking bond distance (d_{S-C}), after 40 iterations for run 1 and run 2. Run 2 was built by constraining the area to the maximum of energy in run 1.

coordinate path. Although in this case choosing a coordinate would be very easy (because the reaction is the breaking of one bond), there are many cases where selecting one distinguished coordinate would be a difficult choice, and the coordinate chosen could turn to be unrepresentative of the MEP. This is one of the advantages of the NEB minimization: the path is minimized without any restriction on the coordinates of the images. It is worth noting that the location of the saddle point (if it exists) should be independent of the particular system of coordinates chosen. However, this is not true for the reaction path; the NEB path should converge to the steepest descents path in whatever coordinate system is used; the user should keep in mind that only in an isoinertial coordinate system is the steepest-descents path equal to the intrinsic reaction path, which is the MEP in the notation we usually use.

In contrast with the results for reaction R1, reaction R2 showed a maximum of energy along the NEB path, as can be seen in Figure 6. This suggests although it does not prove, that the dissociation of CH_3SCH_2O takes place via a saddle point. To characterize this saddle point, we performed a second NEB minimization by limiting the images to the area around that energy maximum. In particular, we built a second initial path using two images from the first run as the final end points of the second run. This second run yielded a

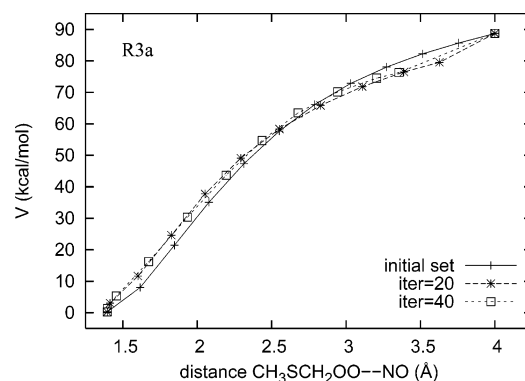


Figure 7. NEB minimization for NO addition to CH_3SCH_2OO radical (reaction R3a). The relative potential energy (vs the addition minimum, CH_3SCH_2OONO) as a function of the forming bond $O-N$ distance is depicted. Three different stages of the minimization are shown: the initial guess, the energies after 20 iterations, and the final energies obtained after 40 iterations.

maximum of energy very close to the true saddle point. Using the geometry of the maximum-energy image as a starting point, we performed a transition-state (TS) search with the Gonzalez-Schlegel algorithm⁵⁵ as implemented in *Gaussian03*,⁴⁴ and it converged to the saddle point after only three cycles. The maximum-energy point in the second NEB run was 8.4 kcal/mol above reactants, while the real saddle point is at 7.8 kcal/mol; the normal mode associated with the reaction coordinate ($C-S$ stretching) has a frequency of 430i cm^{-1} , while at the saddle point it is 364i cm^{-1} .

3.2.2. $CH_3SCH_2OO + NO \rightarrow CH_3SCH_2O + NO_2$. We studied reaction R3 by assuming that it takes place in two steps: (1) the NO addition to the radical to form a stable complex and (2) the CH_3SCH_2OONO dissociation to form NO_2 and CH_3SCH_2O , whose dissociation is discussed above. The initial guess of images for both reaction R3a and reaction R3b were built by linear interpolation between the stationary point representing the addition complex (CH_3SCH_2OO-NO) and a “reactant-like” and “product-like” geometry, respectively. For the NO addition we used a “reactant-like” structure where the forming $O-N$ bond had a length of 4 Å; the “product-like” geometry for the CH_3SCH_2OONO dissociation was represented by a structure with a breaking $O-O$ bond of length 4 Å. These two end points were not optimized.

In Figure 7 the NEB minimization for the NO addition is shown. It can be observed that NO addition takes place via a barrierless association. We did not perform any refinements for this path because no saddle point is expected when the potential energy profile along the reaction path is monotonic. Figure 8 shows the successive NEB minimizations for reaction R3b. As the first run suggested that this dissociation takes place via a saddle point, we ran more NEB cycles in order to get closer to that point. Each successive run was performed by constraining the search to the maximum-energy area. After 4 runs, we used the highest energy image as the initial guess for a conventional TS search. By using the Gonzalez-Schlegel algorithm⁵⁵ as implemented in *Gaussian03*⁴⁴ we did succeed in finding the saddle point for reaction R3b. Comparing the highest-energy image in the

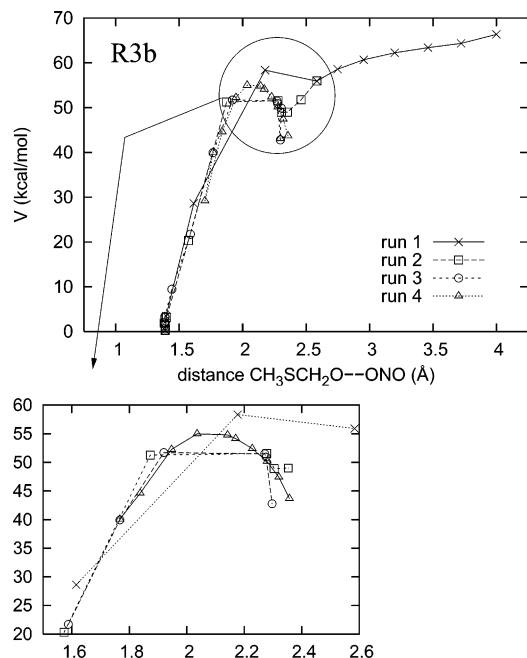


Figure 8. NEB minimization for $\text{CH}_3\text{SCH}_2\text{OONO}$ dissociation (reaction R3b). The relative potential energy (vs the minimum, $\text{CH}_3\text{SCH}_2\text{OONO}$) as a function of the breaking bond O–O distance is depicted. The results for four consecutive runs are shown. A zoom in the highest-energy area is also depicted.

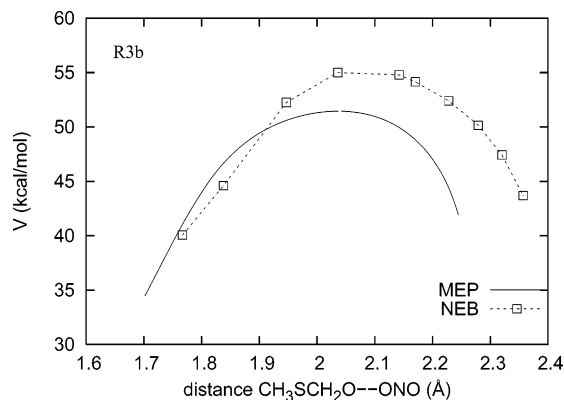


Figure 9. A comparison between the energy along the NEB and the energy along the MEP for $\text{CH}_3\text{SCH}_2\text{OONO}$ dissociation (reaction R3b) is shown. The relative potential energy along the path (vs the minimum, $\text{CH}_3\text{SCH}_2\text{OONO}$) is depicted vs the breaking bond O–O distance.

fourth NEB run with the saddle point shows that the point was geometrically very close to the saddle point. For example, the breaking O–O bond was 2.04 Å in both cases. However, the highest-energy image had two additional imaginary frequencies, besides the one associated with the reaction coordinate. Those additional frequencies were eliminated during the Gonzalez-Schlegel minimization. The value of the imaginary frequency for the mode associated with the reaction coordinate went from 367i to 189i cm^{-1} . After characterizing the saddle point we computed the MEP in order to compare the potential energy along the MEP to that along the NEB path. This comparison is shown in Figure 9. The differences between these two paths show that the NEB minimizations did not converge to the MEP mainly because the minimization was not completed. It is important

to remark here that the MEP could be computed because we previously obtained the saddle point by using the NEB algorithm.

In contrast, when using a distinguished reaction coordinate, we could not characterize the saddle point. Since a saddle point is needed to start the MEP calculation, using the NEB algorithm was a necessary starting point.

The main aim of the studies reported in this section was to obtain a global view for each reaction studied and to characterize the saddle points (if they exist). If we wanted to converge the NEB to the MEP we would need to use more images along the NEB and more cycles for the minimization (all our minimizations were stopped after 40 cycles).

4. Conclusions

The Nudged Elastic Band method was originally proposed for condensed-phase systems and is particularly useful for such cases. We have shown here that it can also be very useful for gas-phase reactions, and we have implemented it for this kind of application in the MULTILEVEL²⁷ program. Three options are included for the tangent vector, and users can choose among several options for other variables as well. On the basis of our studies we recommend default values that can guide the user in preliminary searches.

In some cases the optimum parameters to be used depend on the purpose of the calculation. For example, Figures 2–5 are not smooth due to the small number of images used. We did not employ more images because in those cases we were carrying out exploratory work. Later, in Figures 6 (bottom) and 8, we increased the number of images used (we concentrated additional images in the more interesting region). In this way, we obtained a smoother path.

The performance of the code has been illustrated for reactions involved in the DMS chemistry of the atmosphere. We characterized the paths for those reactions to show that one can elucidate whether they take place via a saddle point. For reactions where the profile showed a maximum in the potential energy profile, we characterize the saddle point by performing an iterative NEB minimization followed by a saddle-point search. One can characterize an unknown reaction in a systematic fashion by first doing a general NEB minimization for a broad whole range of the reaction coordinate and then constraining the search to the most interesting regions.

Acknowledgment. This work was supported in part by the U.S. Department of Energy, Office of Basic Energy Sciences. N.G.G. would like to acknowledge the Generalitat de Catalunya for the BE fellowship received.

References

- (1) Truhlar, D. G.; Steckler, R.; Gordon, M. S. *Chem. Rev.* **1987**, 87, 217.
- (2) *Supercomputer Algorithms for Dynamics and Kinetics of Small Molecules*; Laganà, A., Ed.; Kluwer: Dordrecht, 1989; p 105.
- (3) McKee, M. L.; Page, M. *Rev. Comput. Chem.* **1993**, IV, 35.
- (4) Page, M. *Computer Phys. Commun.* **1994**, 84, 115.

- (5) *The Reaction Path in Chemistry: Current Approach and Perspectives*; Heidrich, D., Ed.; Kluwer: Dordrecht, 1995.
- (6) Schlegel, H. B. *J. Comput. Chem.* **2003**, *24*, 1515.
- (7) Halgren, T. A.; Lipscomb, W. N. *Chem. Phys. Lett.* **1977**, *49*, 225.
- (8) Melissas, V. S.; Truhlar, D. G. *J. Chem. Phys.* **1992**, *96*, 5758.
- (9) Rothman, M. J.; Lohr, J. L.; Ewig, C. S.; Wazer, van J. R. In *Potential Energy Surfaces and Dynamical Calculations*; Truhlar, D. G., Ed.; Plenum: New York, 1979; pp 653–660.
- (10) Cerjan, C. J.; Miller, W. H. *J. Chem. Phys.* **1981**, *75*, 2800.
- (11) Banerjee, A.; Adams, N.; Simons, J.; Shepard, R. *J. Phys. Chem.* **1985**, *89*, 52.
- (12) Baker, J. *J. Comput. Chem.* **1985**, *7*, 385.
- (13) Culot, P.; Dive, G.; Nguyen, V. H.; Ghuysen, J. M. *Theor. Chim. Acta* **1992**, *82*, 189.
- (14) Quapp, W. *Chem. Phys. Lett.* **1996**, *253*, 286.
- (15) Mills, G.; Jónsson, H. *Phys. Rev. Lett.* **1994**, *72*, 1124.
- (16) Mills, G.; Jónsson, H.; Schenter, G. K. *Surf. Sci.* **1995**, *324*, 305.
- (17) Gillilan, R. E.; Wilson, K. R. *J. Chem. Phys.* **1992**, *97*, 1757.
- (18) Henkelman, G.; Uberuaga, B. P.; Jónsson, H. *J. Chem. Phys.* **2000**, *113*, 9901.
- (19) Jónsson, H.; Mills, G.; Jacobsen, K. W. In *Classical and Quantum Dynamics in Condensed Phase Simulations*; Berne, B. J., Cicotti, G., Coker, D. F., Ed.; World Scientific: Singapore, 1998; pp 385–404.
- (20) Henkelman, G.; Jónsson, H. *J. Chem. Phys.* **2000**, *113*, 9978.
- (21) Crehuet, R.; Field, M. *J. Chem. Phys.* **2003**, *118*, 9563.
- (22) Alfonso, D. R.; Jordan, K. D. *J. Comput. Chem.* **2003**, *24*, 990.
- (23) Chu, J.-W.; Trout, B.; Brooks, B. *J. Chem. Phys.* **2003**, *119*, 12708.
- (24) Peters, B.; Heyden, A.; Bell, A. T.; Chakraborty, A. *J. Chem. Phys.* **2004**, *120*, 7877.
- (25) Besal, E.; Bofill, J. M. *Theor. Chem. Acc.* **1998**, *100*, 265.
- (26) Quapp, W.; Hirsch, M.; Imig, O.; Heidrich, D. *J. Comput. Chem.* **1998**, *19*, 1087.
- (27) Zhao, Y.; Rodgers, J.; Lynch, B.; González-García, N.; Fast, P.; Pu, J.; Chuang, Y.; Truhlar, D. *MultiLevel4.1*; University of Minnesota: Minneapolis, MN, 2005.
- (28) Charlson, R. J.; Lovelock, J. E.; Andreae, M. O.; Warren, S. G. *Nature* **1987**, *326*, 655.
- (29) González-García, N.; González-Lafont, A.; Lluch, J. M. *J. Comput. Chem.* **2005**, *26*, 569.
- (30) González-García, N.; González-Lafont, A.; Lluch, J. M. *J. Phys. Chem. A* **2006**, *110*, 788.
- (31) *Gaussian 98, revision A.6 and A.7*; Gaussian, Inc.: Pittsburgh, PA, 1998.
- (32) Johnson, D. *Phys. Rev. B* **1988**, *38*, 12807.
- (33) Chen, Z. *Theor. Chim. Acta* **1989**, *75*, 481.
- (34) Corchado, J. C.; Chuang, Y.-Y.; Fast, P. L.; Villà, J.; Hu, W.-P.; Liu, Y.-P.; Lynch, G. C.; Nguyen, K. A.; Jackels, C. F.; Melissas, V. S.; Lynch, B. L.; Rossi, I.; Coitiño, E. L.; Fernández-Ramos, A.; Pu, J.; Albu, T. V.; Steckler, R.; Garret, B. C.; Isaacson, A. D.; Truhlar, D. G. *PolyRate9.3*; University of Minnesota: Minneapolis, MN, 2003.
- (35) Fletcher, R. *Practical Methods of Optimization*; Wiley: Chichester, 1991.
- (36) Broyden, C. *J. Inst. Math. App.* **1970**, *6*, 76.
- (37) Fletcher, R. *Comput. J. (UK)* **1970**, *13*, 317.
- (38) Goldfarb, D. *Math. Comput.* **1970**, *24*, 23.
- (39) Shannon, D. *Math. Comput.* **1970**, *24*, 647.
- (40) Wittbrodt, J.; Schlegel, H. *J. Mol. Struct. (THEOCHEM)* **1997**, *398*, 55.
- (41) Bofill, J. *J. Comput. Chem.* **1994**, *15*, 1.
- (42) Anglada, J.; Bofill, J. *J. Comput. Chem.* **1998**, *19*, 349.
- (43) Powell, M. *Math. Program* **1971**, *1*, 26.
- (44) Frisch, M. J.; Trucks, G. W.; Schlegel, H. B.; Scuseria, G. E.; Robb, M. A.; Cheeseman, J. R.; Montgomery, J. A., Jr.; Vreven, T.; Kudin, K. N.; Burant, J. C.; Millam, J. M.; Iyengar, S. S.; Tomasi, J.; Barone, V.; Mennucci, B.; Cossi, M.; Scalmani, G.; Rega, N.; Petersson, G. A.; Nakatsuji, H.; Hada, M.; Ehara, M.; Toyota, K.; Fukuda, R.; Hasegawa, J.; Ishida, M.; Nakajima, T.; Honda, Y.; Kitao, O.; Nakai, H.; Klene, M.; Li, X.; Knox, J. E.; Hratchian, H. P.; Cross, J. B.; Bakken, V.; Adamo, C.; Jaramillo, J.; Gomperts, R.; Stratmann, R. E.; Yazyev, O.; Austin, A. J.; Cammi, R.; Pomelli, C.; Ochterski, J. W.; Ayala, P. Y.; Morokuma, K.; Voth, G. A.; Salvador, P.; Dannenberg, J. J.; Zakrzewski, V. G.; Dapprich, S.; Daniels, A. D.; Strain, M. C.; Farkas, O.; Malick, D. K.; Rabuck, A. D.; Raghavachari, K.; Foresman, J. B.; Ortiz, J. V.; Cui, Q.; Baboul, A. G.; Clifford, S.; Cioslowski, J.; Stefanov, B. B.; Liu, G.; Liashenko, A.; Piskorz, P.; Komaromi, I.; Martin, R. L.; Fox, D. J.; Keith, T.; Al-Laham, M. A.; Peng, C. Y.; Nanayakkara, A.; Challacombe, M.; Gill, P. M. W.; Johnson, B.; Chen, W.; Wong, M. W.; Gonzalez, C.; Pople, J. A. *Gaussian 03, Revision C.02*; Gaussian, Inc.: Wallingford, CT, 2004.
- (45) Lynch, B. J.; Fast, P. L.; Harris, M.; Truhlar, D. G. *J. Phys. Chem. A* **2000**, *104*, 4811.
- (46) Lynch, B. J.; Truhlar, D. G. *J. Phys. Chem. A* **2001**, *105*, 2936.
- (47) Parthiban, S.; Oliveira, G. D.; Martin, J. M. L. *J. Phys. Chem. A* **2001**, *105*, 895.
- (48) Claes, L.; François, J. P. F.; Deleuze, M. S. *J. Am. Chem. Soc.* **2002**, *124*, 7563.
- (49) Claes, L.; François, J. P. F.; Deleuze, M. S. *J. Am. Chem. Soc.* **2003**, *125*, 7129.
- (50) Iron, M. A.; Lo, H. C.; Martin, J. M. L.; Keinan, E. *J. Am. Chem. Soc.* **2002**, *124*, 7041.
- (51) Frisch, M. J.; Pople, J. A.; Binkley, J. S. *J. Chem. Phys.* **1984**, *80*, 3265.
- (52) Hehre, W. J.; Radom, L.; R. Schleyer, P. v. R.; Pople, J. A. *Ab Initio Molecular Orbital Theory*; Wiley: New York, 1986.
- (53) Wayne, R. P. *Chemistry of Atmospheres*, 3rd ed.; Oxford University Press: New York, 2000.
- (54) Resende, S. M.; Almeida, W. B. D. *Phys. Chem. Chem. Phys.* **1999**, *1*, 2953.
- (55) González, C.; Schlegel, H. B. *J. Phys. Chem.* **1990**, *94*, 5523.